

Influence factors and prediction model of enstrophy dissipation from the tip leakage vortex in a multiphase pump

Zekui Shu (✉ shuzekui@126.com)

Xihua University <https://orcid.org/0000-0002-3087-3887>

Guangtai Shi

Xihua University

Xin Yao

Xihua University

Guodong Sun

Xihua University

Sijia Tao

Xihua University

Research Article

Keywords: Multiphase pump, Tip leakage vortex, Enstrophy dissipation, Simple regression model, Multiple nonlinear regression model

Posted Date: April 4th, 2022

DOI: <https://doi.org/10.21203/rs.3.rs-1417207/v1>

License:  This work is licensed under a Creative Commons Attribution 4.0 International License.

[Read Full License](#)

Influence factors and prediction model of enstrophy dissipation from the tip leakage vortex in a multiphase pump

Zekui Shu^{1, 3}, Guangtai Shi^{1, 2, 3, a)}, Xin Yao^{1, 3}, Guodong Sun^{1, 3}, Sijia Tao^{1, 3}

¹Key Laboratory of Fluid Machinery and Engineering (Xihua University), Sichuan Province, Chengdu 610039, China

²State Key Laboratory of Hydrosience and Engineering and Department of Energy and Power Engineering, Tsinghua University, Beijing 100084, China

³Key Laboratory of Fluid and Power Machinery (Xihua University), Ministry of Education, Chengdu 610039, China

^{a)}Author to whom correspondence should be addressed: sgtaixh@126.com.

ABSTRACT: In a multiphase pump, tip clearance is the required distance between the blade tip and the pump body wall of the impeller, and can regulate tip leakage vortex (TLV), causing unstable flow and energy dissipation. However, there are few studies on the energy dissipation caused by the TLV. In the present work, the enstrophy dissipation theory is innovatively applied to quantitatively study the energy dissipation of the TLV. The flow rate (Q), tip clearance (Rtc), and inlet gas void fraction ($IGVF$) play a crucial role in affecting the enstrophy dissipation of the TLV. The results suggest that increasing Q , Rtc , and $IGVF$ significantly exacerbate the TLV pattern and raise the TLV scale, which gradually raises volume enstrophy dissipation and decreases wall enstrophy dissipation. The maximum pressure load in the impeller occurs at the 0.5 chord, where a strong TLV is generated, leading to significant enstrophy dissipation. As the flow rate increases, the separation angle between the primary TLV (PTLV) trajectory and the blade gradually decreases, and widely dispersing the enstrophy dissipation near the shroud. However, as the tip clearance increases, the tip-separated vortex (TSV) scale increases and extends to the suction surface, raising the velocity gradient. Besides, as the $IGVF$ increases, the secondary TLV (STLV) develops from a continuous sheet vortex to a scattered strip vortex, increasing the pressure fluctuation intensity. Considering the flow rate, tip clearance, and $IGVF$ as independent variables, simple and multiple nonlinear regression models for the enstrophy dissipation are established.

KEYWORDS: Multiphase pump, Tip leakage vortex, Enstrophy dissipation, Simple regression model, Multiple nonlinear regression model

Nomenclature			
μ	Dynamic viscosity [Pa·s]	Q	Flow rate [m ³ ·h ⁻¹]
S_r	Strain rate tensor [—]	Rtc	Tip clearance [mm]
p	Pressure [Pa]	τ	Shear stress [N]
\bar{u}	Circumferential velocity [m·s ⁻¹]	v	Velocity [m·s ⁻¹]
$\bar{\omega}$	Vorticity [s ⁻¹]	Q_c	Vortex intensity [s ⁻²]
Φ_k	Volumetric enstrophy dissipation rate [W·m ⁻³]	Acronyms	
Φ_{ave}	Average enstrophy dissipation rate [W·m ⁻³]		
Φ_{ful}	Fluctuating enstrophy dissipation rate [W·m ⁻³]	TLV	Tip leakage vortex
Φ_{wall}	Wall enstrophy dissipation rate [W·m ⁻²]	PTLV	Primary tip leakage vortex
P_{ens}	Total enstrophy dissipation power [W]	STLV	Secondary tip leakage vortex
P_{ave}	Average enstrophy dissipation power [W]	TSV	tip separated vortex
P_{ful}	Fluctuating enstrophy dissipation power [W]	LV	Leading-edge vortex
P_k	Volumetric enstrophy dissipation power [W]	TV	Trailing-edge vortex
P_{wall}	Wall enstrophy dissipation power [W]	IGVF	Inlet gas void fraction
I_{PF}	Pressure fluctuation intensity [—]	PS	Pressure surface
ρ	Density [kg·m ⁻³]	SS	Suction surface

1 INTRODUCTION

The consumption of oil and gas resources accounts for up to 80% of the energy used to power global social production. After many years of exploitation and use, the onshore energy reserves are insufficient to meet future modern industrial production needs.^{1,2} Experts all over the world have shifted their attention to the rich oil and gas resources beneath the oceans, prioritizing the efficient and convenient transportation of subsea oil and gas resources.³ Compared to traditional oil and gas separation transportation technology, multiphase transportation simplifies the transportation process and reduces maintenance costs. Multiphase pumps, as the core equipment of multiphase transportation technology, have been optimized and improved significantly in recent years, not only enhancing the production efficiency but also significant economic benefits.⁴⁻⁶ A tip leakage flow is generated in a multiphase pump due to the pressure difference and relative movement between the blade tip and the pump body wall of the impeller, and this interacts with the main flow to form the complex TLV.⁷ The TLV destabilizes the flow and induces cavitation, vibration, and noise, all of which deteriorate the hydraulic mechanical performance.⁸⁻¹⁰

Many scholars have carried out extensive research on the multiphase pump, including gas-liquid two-phase flow¹¹, bubble motion¹², cavitation¹³ and energy conversion¹⁴. Zhang *et al.*¹⁵⁻¹⁷ noticed a visual change in the flow pattern of gas in a multiphase pump, with distinct isolated bubbles, bubbly flow, gas pockets, and segregated gas flow stages as the *IGVF* increased. They discovered that the bubble diameter is closely related to the *IGVF* and flow speed. Zhang *et al.*^{18,19} examined the bubble movement in the pump and reported that the bubbles moved and aggregated

from the pressure surface (PS) to the suction surface (SS) of the blade, and the bubble volumes are significantly affected by the blade wall. Shi *et al.*²⁰ found that under gas-liquid two-phase conditions, the impeller power degraded, and the energy conversion performance was worst.

However, there have been only a few studies on the TLV in multiphase pumps.^{21,22} Previous studies²³⁻²⁶ on the TLV in turbomachinery have been conducted by experiments and numerical simulation. Wu *et al.*²⁷⁻²⁹ observed the formation process of the TLV in the tip clearance area of a jet pump using stereo particle image velocimetry. The vortex sheet formed from unsteady vortex filaments in the tip region intertwine to form a TLV structure. The circumferentially rotating filaments become rolled up during the shedding of the TLV and revolve around the TLV with their axes perpendicular to the TLV axis. Liu *et al.*^{30,31} simulated the flow characteristics of the TLV in a mixed flow pump and experimentally validated the simulation results. The temporal-spatial evolution of the TLV was divided into three stages, splitting, developing, and merging, and relative vortex stretching in the Z direction was discovered to be the primary source of splitting and shedding in the PTLV. A theoretical model for accurately predicting the PTLV trajectory was also proposed.³² Cheng *et al.*³³⁻³⁵ used the large-eddy simulation framework to study the cavitation flow of the TLV generated by the NACA0009 hydrofoil. They classified the spatial evolution of the TLV cavitation flow into three stages: development, fusion, and dissipation, and discovered that the TLV cavitation had a significant influence on the local flow pattern and turbulence distribution. Besides, tip clearance modification is widely used in hydrofoil research, for example, T-shape tip clearance,³⁶ C-shape tip clearance,³⁷ double-curved-hole,³⁸ to reduce TLV flow loss³⁹ and noise production, improving cavitation performance.^{40,41}

Meticulous research survey indicated that the flow rate³⁰, tip clearance²¹, and $IGVF$ ²² play a crucial role in affecting the flow pattern of the TLV and cause energy dissipation. Some studies⁴³⁻⁴⁶ have optimized the performance of pumps by quantitatively analyzing the position and mode of energy loss using entropy production theory. Ji *et al.*^{47,48} found that the high energy dissipation in the impeller of the mixed-flow pump is caused by TLV, secondary flow vortex, and stall vortex. As the tip clearance increases, the intensity and scale of the TLV surge, sharply increasing the total entropy generation. The dissipation of vortex energy is termed enstrophy, for which a theoretical formula was derived by Wu *et al.*⁴⁹ derived from the kinetic energy transport equation, providing a theoretical basis for the study of turbulent enstrophy dissipation.⁵⁰ The relationship between enstrophy and energy dissipation rate in turbulent flow has been investigated, with enstrophy in the boundaries of objective Eulerian coherent structures produced by vortex stretching, and the enstrophy is transferred through the structure boundaries by viscous diffusion.⁵¹⁻⁵³ Lin *et al.*⁵⁴ effectively diagnosed the flow characteristics of a turbine pump using enstrophy dissipation theory and determined the region of high enstrophy dissipation. Therefore, enstrophy dissipation theory is applied to the energy dissipation generated by the TLV, and the position, form, and dissipation rate can be determined.

Overall, most of the previous studies have been focused on the flow pattern of the TLV in a

multiphase pump. However, the studies on the influence factors of the TLV are rarely reported, and there is a lack of systematic research on energy dissipation caused by the TLV. In the present study, the enstrophy dissipation theory is innovatively applied to study the energy dissipation of the TLV quantitatively. The effects of the flow rate, tip clearance, and *IGVF* on the vorticity, flow pattern, pressure load, and enstrophy dissipation are analyzed in the impeller. A simple nonlinear regression model was established considering the influencing factors that accurately predict the enstrophy dissipation of the TLV. Finally, the enstrophy dissipation law under the interaction of multiple factors is further explored, and a multiple nonlinear regression model is established. The results presented provide a theoretical basis for calculating the energy dissipation of the TLV accurately in multiphase pumps.

2 PHYSICAL MODEL AND GRID GENERATION

2.1 Physical model

The research object is a self-designed single-stage multiphase pump, the main components of which include the impeller, diffuser, pump body, and inlet and outlet pipeline. The main design parameters are listed in Table I. The impeller is made of stainless steel and can withstand abrasion while ensuring efficient pressurization. The diffuser and pump body are made of transparent glass, which is conducive to capturing the flow pattern inside the multiphase pump. The test prototype is shown in Fig. 1. A three-dimensional model for the computational domain, including the inlet, impeller, diffuser, and outlet domains, is developed using UG software (Fig. 2(a)). The impeller inlet and diffuser outlet are of sufficient lengths to ensure a steady flow of fluid into and out of the pressurization unit. In addition, five pressure monitoring points are arranged on the PS of the impeller and diffuser, namely, IPS_1 – IPS_5 and DPS_1 – DPS_5 , respectively, as shown in Fig. 2(b).

TABLE I. Main design parameters.

Parameter	Symbol	Value	Units
Design flow rate	Q_d	100	$\text{m}^3\cdot\text{h}^{-1}$
Design speed	n	3600	rpm
Number of impeller blades	Z_1	3	—
Number of diffuser blades	Z_2	11	—
Hub/shroud ratio	d	0.7	—
Inner diameter	D	161	mm



FIG. 1. Test prototype of the multiphase pump.

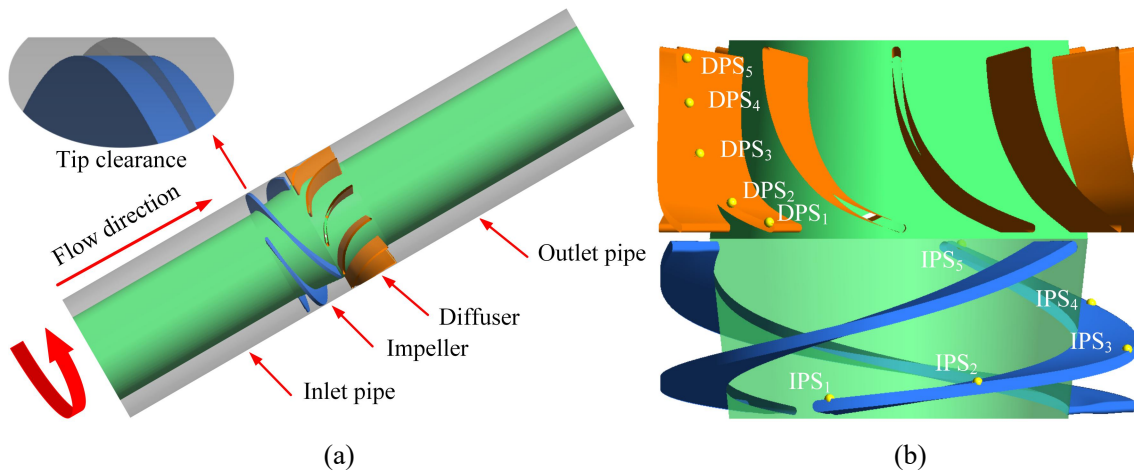


FIG. 2. Schematic diagram of computational domain and monitoring points. (a) Computational domain and (b) monitoring points.

2.2 Grid generation

A high-quality structural grid is critical for numerical simulations to be reliable and accurate. The grid covering the computational domain is arranged using a hexahedral structure, as shown in Fig. 3. The boundary layer grid near the wall is refined to ensure better quality, and the O-topology is used to surround the blade. In particular, 30 and 25 layers are arranged in the radial and circumferential directions of the tip clearance region, respectively. The value of the Y^+ is maintained at less than 60 in the impeller. The scalable wall function is used as a wall function, which is contributed to improving the computing accuracy.

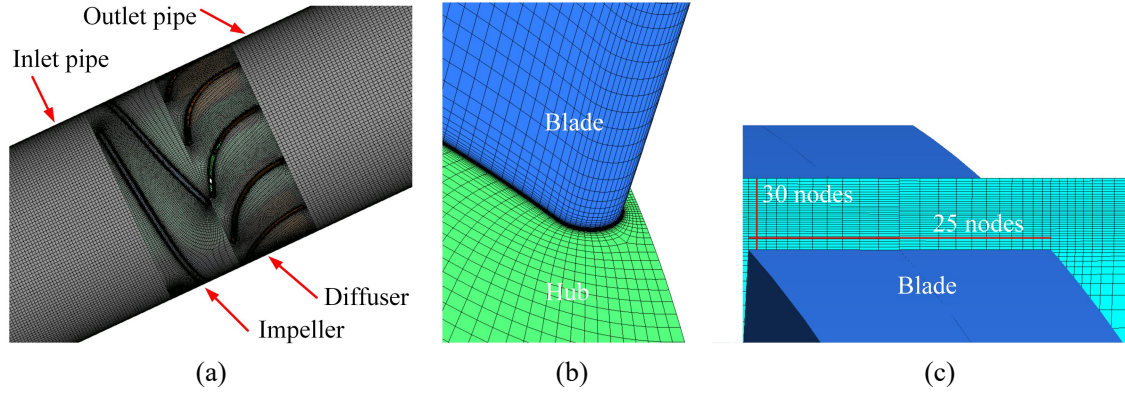


FIG. 3. Computational grid. (a) Whole computational domain, (b) impeller blade, and (c) tip clearance.

3 NUMERICAL COMPUTATION METHOD

3.1 Simulation settings

The numerical simulations of a multiphase pump were performed using ANSYS CFX. The Eulerian-Eulerian model is used to calculate gas-liquid two-phase flow.⁵⁵ The gas and liquid in the two-phase model were air and water, respectively, which are maintained at 25°C. The SST $k - \omega$ turbulence model was used for the liquid phase, as it can effectively predict the flow separation point, separation region, and TLV trajectory.^{31,32} The gas-phase diameter was set to 0.1 mm, and the Dispersed Phase Zero Equation was used as its turbulence model.⁴⁷ The rotational speed of the impeller was set to 3000 rpm in the pump, and the shroud of the impeller was set to counter-rotating mode in the relative coordinate system. Velocity inlet, pressure outlet, and no-slip wall conditions were imposed at the boundaries. The convergence precision was 10^{-5} . In the steady simulation, the number of steps was set to 3000, and Frozen Rotor was used for the rotor-stator interface. The steady simulation results were taken as the initial value of the transient simulations to accelerate the convergence. The Computational time of transient simulation was 0.4s i. e. the time it takes for an impeller revolution 20T. Meanwhile, transient frozen rotor was used for the rotor-stator interface.

3.2 Grid independence study

The grid independence of a multiphase pump with a tip clearance of 1.0 mm was verified at the design flow rate. Five grid resolutions were selected for the simulations, and the results are presented in Table II. As the grid resolution increases, the head and efficiency of the pump increase and tend to become stable. The difference in the head and efficiency between grids 4 and 5 is very small; thus, the effect of the grid resolution variation on the calculation results can be neglected. Therefore, given the computation time and accuracy requirements, we selected grid 4 for the subsequent simulations.

TABLE II. Grid independence study.

Component	Grid 1	Grid 2	Grid 3	Grid 4	Grid 5
Total number of cells	2,327,229	2,888,523	3,499,716	3,902,631	6,069,444
P_{ens} (W)	1518.13	1580.21	1609.96	1628.45	1635.23
η (%)	43.35	44.49	44.60	45.41	45.58
P_{ens} / P_{ens1}	1	1.0409	1.0605	1.0727	1.0771
η/η_1	1	1.0165	1.0218	1.0327	1.0384

3.3 Time step independence study

Although smaller time steps capture unsteady information more accurately, they consume more computing resources.¹¹ Thus, time steps of 5.56×10^{-5} s, 1.11×10^{-4} s, and 1.67×10^{-4} s corresponding to 360, 180, and 120 steps per revolution, respectively, were used to conduct simulations. Figure 4 shows the time histories of monitoring point DPS_1 under different time steps. The fluctuations in pressure at this monitoring point are almost similar under the different time steps, indicating that the influence of the time step size on the results is negligible. Ultimately, a time step of 1.11×10^{-4} s was selected for the transient simulations.

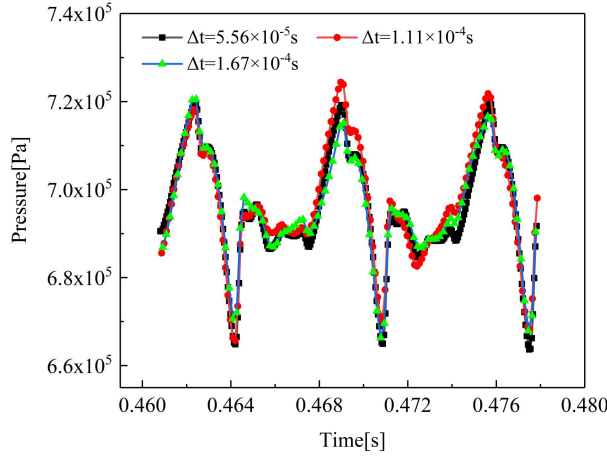


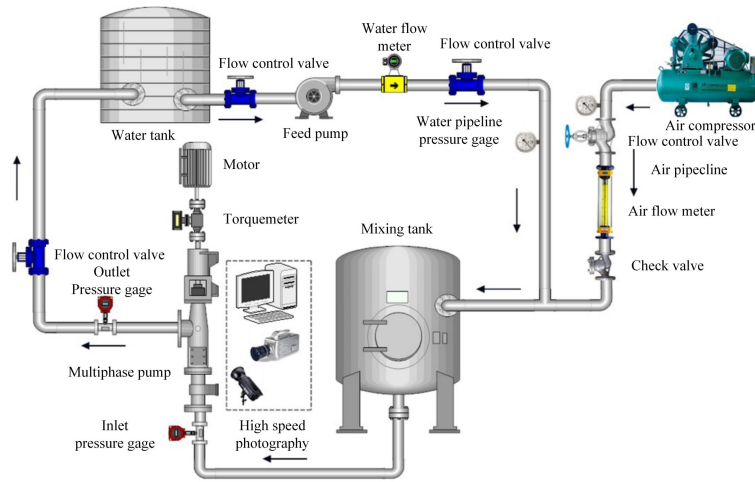
FIG. 4. Time step independence study.

3.4 Verification with experiment

Experimentation was conducted using a test system and multiphase equipment. As the system runs, air and water enter the mixing tank through the respective pipelines, and the valve is controlled to homogeneously mix the gas and liquid in different proportions. The flow pattern in the impeller was captured with photographs at various points with a high-speed camera. The test system is shown in Fig. 5.



(a)



(b)

FIG. 5. Test system of the multiphase equipment. (a) Photograph of the test system and (b) schematic of the test system.

The external characteristics of a multiphase pump with a tip clearance of 1.0 mm were tested at a rotational speed of 3000 rpm, and test values for the head, efficiency, and output power were obtained. The simulation values for the head, efficiency, and output power of the pump simulated using CFD were determined. The results of the test and simulation with external characteristic lines are shown in Fig. 6 for different flow rates of 60–120 m³·h⁻¹. The numerical simulation results are in good agreement with those of the experiments. Thus, it can be concluded that the numerical simulation scheme established in this study accurately predicts the energy performance of the multiphase pump.

Five different *IGVFs* (0%, 5%, 10%, 15%, and 20%) were selected to study the internal flow in the pump under the design flow rate condition. The flow patterns of the test results are compared with the vortex intensity ($Q_c = 1.5 \times 10^6 \text{ s}^{-2}$) of the numerical simulations in Fig. 7. Under the water condition, the vortex scales are modest in the impeller, while the PTLV and trailing-edge vortex (TV)

are clearly apparent. The scales of the TSV and STLW increase significantly as the *IGVF* increases, and the STLW splits into a scattered strip structure. When the *IGVF* reaches 20%, the TLV wraps around the gas phase to fill the flow passage. The vortex pattern of the experimental flow fields is highly consistent with that of the numerical simulations under different conditions.

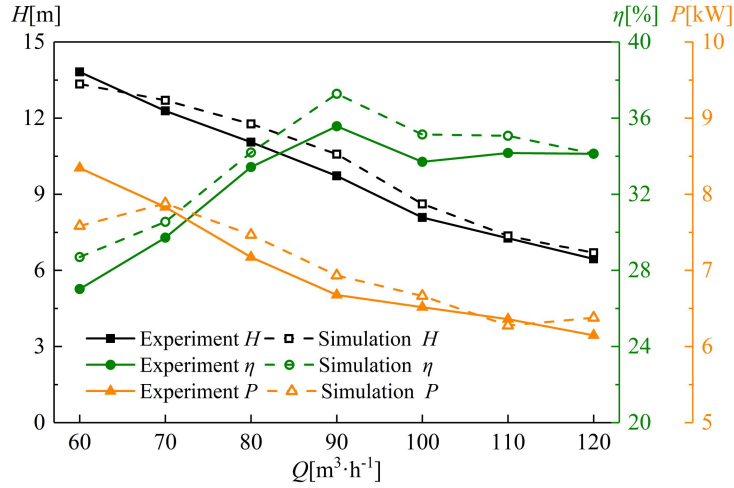


FIG. 6. External characteristic lines of a multiphase pump.

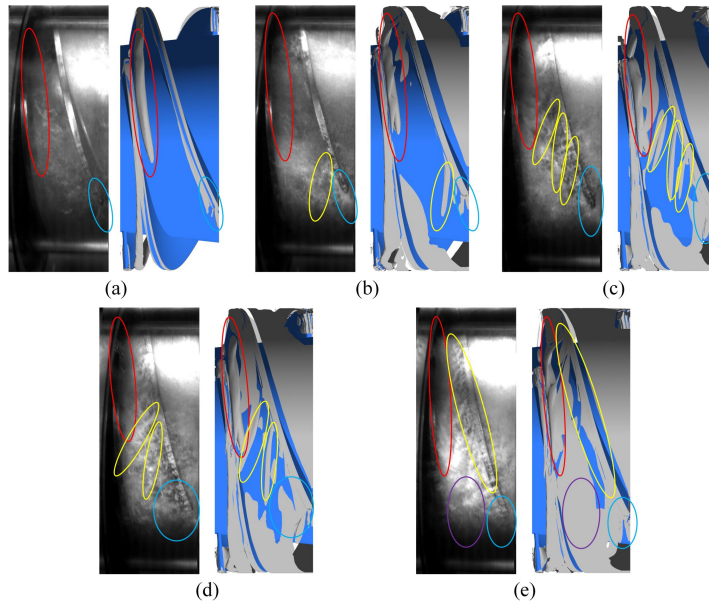


FIG. 7. Flow pattern of the TLV. (a) *IGVF*=0, (b) *IGVF*=5%, (c) *IGVF*=10%, (d) *IGVF*=15% and (e) *IGVF*=20%. The red circle marks the PTLV, the yellow circle marks the STLW, the blue circle marks the TV, and the purple circle marks the vortex in the passage.

4 ENSTROPY DISSIPATION THEORY

To quantitatively analyze the influence of the tip leakage flow on the energy loss of a pump, we introduce the kinetic energy transport equation:

$$\rho \frac{DE}{Dt} = \rho f \cdot \bar{u} + (\nabla \cdot \bar{u})p + \nabla \cdot (S_T \cdot \bar{u}) - \phi. \quad (1)$$

In Eq. (1), S_T is the stress tensor, given by $S_T = 2\mu S_r - (p - 2/3 \cdot (S_T \cdot \bar{u}))I$, where μ , S_r , p , \bar{u} , and I denote the dynamic viscosity, strain tensor rate, pressure, circumferential velocity, and unit tensor, respectively. ϕ is the viscosity dissipation, expressed as $\phi = -2\mu(\nabla \cdot \bar{u})^2 / 3 + 2\mu S_r$. If the compressibility of the fluid is ignored, ϕ is written as

$$\phi = \mu |\bar{\omega}|^2 - 2\mu \nabla \cdot ((\nabla \cdot \bar{u})I - \nabla \bar{u}^T) \cdot \bar{u}, \quad (2)$$

where $\bar{\omega}$ is the vorticity. On substituting Eq. (2) in Eq. (1) and ignoring the effect of the body force, the kinetic energy equation of an incompressible fluid is obtained as follows:

$$\rho \frac{DE}{Dt} = -\nabla \cdot (p\bar{u}) - \nabla \cdot (\mu \bar{\omega} \times \bar{u}) - \mu |\bar{\omega}|^2. \quad (3)$$

In Eq. (3), $\nabla \cdot (p\bar{u})$ represents the work done by pressure on the fluid, called the *pressure propulsion work*. $\nabla \cdot (\mu \bar{\omega} \times \bar{u})$ denotes the nonlinear effects of vorticity and velocity on a viscous fluid. The third term, $\mu |\bar{\omega}|^2$, reflects the dissipation effect of the fluid viscosity and vorticity field on kinetic energy, which is called the *enstrophy dissipation rate*.

The volume enstrophy dissipation rate function is written as

$$\Phi_k = \mu \left[\left(\frac{\partial w}{\partial y} - \frac{\partial v}{\partial z} \right)^2 + \left(\frac{\partial u}{\partial z} - \frac{\partial w}{\partial x} \right)^2 + \left(\frac{\partial v}{\partial x} - \frac{\partial u}{\partial y} \right)^2 \right], \quad (4)$$

where u , v , and w represent the velocity components along the x , y , and z directions in the Cartesian coordinate system, respectively.

For turbulent flow, the volume enstrophy dissipation rate can be divided into two parts:

$$\Phi_k = \Phi_{ave} + \Phi_{ful}, \quad (5)$$

where Φ_{ave} represents the average enstrophy dissipation rate and Φ_{ful} represents the fluctuating enstrophy dissipation rate, which can be given as follows:

$$\Phi_{ave} = \mu \left[\overline{\left(\frac{\partial w}{\partial y} - \frac{\partial v}{\partial z} \right)^2} + \overline{\left(\frac{\partial u}{\partial z} - \frac{\partial w}{\partial x} \right)^2} + \overline{\left(\frac{\partial v}{\partial x} - \frac{\partial u}{\partial y} \right)^2} \right], \quad (6)$$

$$\Phi_{ful} = \mu \left[\overline{\left(\frac{\partial w}{\partial y} - \frac{\partial v}{\partial z} \right)^2} + \overline{\left(\frac{\partial u}{\partial z} - \frac{\partial w}{\partial x} \right)^2} + \overline{\left(\frac{\partial v}{\partial x} - \frac{\partial u}{\partial y} \right)^2} \right]. \quad (7)$$

Kock and Herwig⁵⁶ found that the rate of fluctuating enstrophy dissipation is closely related to the turbulence model used in numerical simulations. Therefore, the fluctuating enstrophy dissipation rate is defined as the product of the fluid density ρ and turbulent dissipation rate ε :

$$\Phi_{ful} = \rho \varepsilon. \quad (8)$$

Energy dissipation on the walls cannot be ignored because of the no-slip conditions. Thus, we adopted the wall enstrophy dissipation rate proposed by Hou *et al.*:⁴³

$$\Phi_{wall} = \tau \cdot \nu. \quad (9)$$

Equations (6), (8), and (9) can be combined to obtain the average enstrophy dissipation power

P_{ave} , fluctuating enstrophy dissipation power P_{ful} , and wall enstrophy dissipation power P_{wall} :

$$P_{ave} = \int_0^V \Phi_{ave} dV, \quad (10)$$

$$P_{ful} = \int_0^V \Phi_{ful} dV, \quad (11)$$

$$P_{wall} = \int_0^S \Phi_{wall} dS. \quad (12)$$

The volume enstrophy dissipation power P_k and total enstrophy dissipation power P_{ens} are given by:

$$P_k = P_{ave} + P_{ful}, \quad (13)$$

$$P_{ens} = P_{ave} + P_{ful} + P_{wall}. \quad (14)$$

5 RESULTS AND DISCUSSION

5.1 Influence of flow rate on enstrophy dissipation

Steady simulations of the multiphase pump were performed at various flow rates to study the influence of the flow rate on the TLV trajectory and further explore the law of enstrophy dissipation. The simulation results of the enstrophy dissipation power are presented in Table III. As illustrated in Fig. 8, the isosurface of the TLV is defined using Q criterion ($Q_c = 1.5 \times 10^6 \text{ s}^{-2}$), and the relative velocity is applied to color the TLV. As the flow rate increases, the leakage flow is enhanced by the impact of the main flow, the flow pattern becomes more disordered, the TLV scale increases, the inlet velocity of the impeller increases, finally enhancing the resistance effect on the PTLV. Since a high-pressure difference is required to generate the PTLV, the initial point of the PTLV gradually moves from the leading edge to the trailing edge of the blade. When the velocity of the main flow is increased gradually, the separation angle between the PTLV trajectory and the blade gradually decreases.

TABLE III. Influence of the flow rate on the enstrophy dissipation power.

Number	$Q[\text{m}^3 \cdot \text{h}^{-1}]$	$Rtc[\text{mm}]$	$IGVF$	$P_k[\text{W}]$	$P_{wall}[\text{W}]$	$P_{ens}[\text{W}]$
1	80	1.0	10%	1038.1	581.60	1619.70
2	85	1.0	10%	1108.95	578.62	1687.57
3	90	1.0	10%	1144.05	575.25	1719.30
4	95	1.0	10%	1223.29	560.32	1783.61
5	100	1.0	10%	1292.44	553.86	1846.30
6	105	1.0	10%	1293.27	549.82	1843.09
7	110	1.0	10%	1293.76	547.11	1840.87

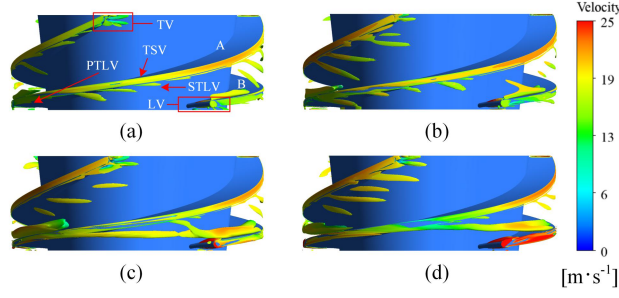


FIG. 8. Flow pattern of the TLV. (a) $80 \text{ m}^3\cdot\text{h}^{-1}$, (b) $90 \text{ m}^3\cdot\text{h}^{-1}$, (c) $100 \text{ m}^3\cdot\text{h}^{-1}$, and (d) $110 \text{ m}^3\cdot\text{h}^{-1}$.

The gas volume fraction at different spans in the impeller is shown in Fig. 9. The flow pattern is stable near the hub region due to the homogenous dispersion of the gas phase, and the flow becomes more stable with higher flow rates. In particular, a high gas volume fraction area appears at 0.5 span. As the flow rate increases, the flow stability in the middle of the impeller passage deteriorates, leading to the formation of small-scale vortices, which results in the gradual expansion of gas volume fraction. The gas phase near the shroud is closely related to the TLV trajectory, as shown in Fig. 9, and the gas volume fraction is higher at larger vortex scales. Therefore, the leading-edge vortex (LV), STLV, and TV have substantial gas volume fractions at 0.95 span, with the STLV gathering a disproportionately large amount of the gas phase. However, the gas volume fraction in the TLV trajectory is low (area marked in red). The PTLV generated on the SS of the blade is affected by the main flow and propagates toward the hub side in the impeller passage. This movement of the PTLV accumulates the gas phase, leading to the low gas volume fraction area at 0.95 span. In addition, when the flow rate rises, the area of high gas volume fraction near the shroud gradually expands.

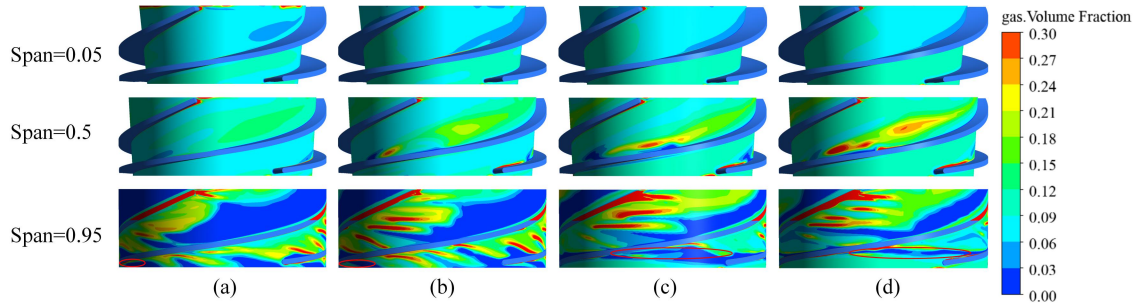


FIG. 9. Distribution of the gas phase at different spans. (a) $80 \text{ m}^3\cdot\text{h}^{-1}$, (b) $90 \text{ m}^3\cdot\text{h}^{-1}$, (c) $100 \text{ m}^3\cdot\text{h}^{-1}$, and (d) $110 \text{ m}^3\cdot\text{h}^{-1}$.

The volume enstrophy dissipation rate Φ_k at 0.95 span is shown in Fig. 10. The distribution of Φ_k maintains a strong correlation with the TLV trajectory in this region. The pressure difference at the blade tip from the leading edge to the trailing edge increases at first, then diminishes, reaching a maximum value at the middle of the blade. A larger pressure difference creates a stronger leakage flow intensity and greater enstrophy dissipation. Therefore, Φ_k is concentrated on the SS of the

blade and coincides with the flow pattern of the TLV. The distribution of Φ_k , in particular, fluctuates as the initial point of the PTLV changes with the flow rate. An increase in the flow rate makes the distribution of Φ_k become more dispersed, and the area of high Φ_k gradually decreases, while the area with medium values of Φ_k gradually expands. The fundamental reason for the dispersive distribution of Φ_k is the presence of small-scale vortices in the impeller passage.

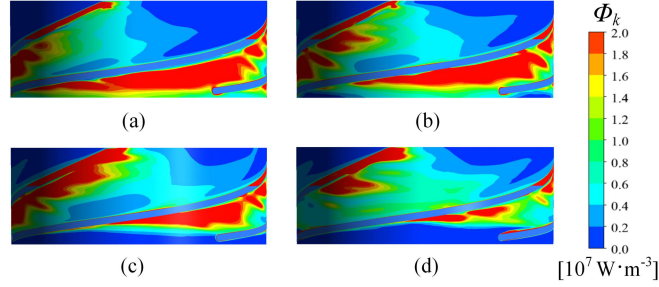


FIG. 10. Distribution of the volume enstrophy dissipation rate at 0.95 span. (a) $80 \text{ m}^3 \cdot \text{h}^{-1}$, (b) $90 \text{ m}^3 \cdot \text{h}^{-1}$, (c) $100 \text{ m}^3 \cdot \text{h}^{-1}$, and (d) $110 \text{ m}^3 \cdot \text{h}^{-1}$.

Figure 11 shows a histogram of the volume enstrophy dissipation power P_k and the wall enstrophy dissipation power P_{wall} , and the variation in the total enstrophy dissipation power P_{ens} . The initial point of the PTLV gradually moves to the trailing edge as the flow rate increases, resulting in a reduction in the tip leakage rate. Moreover, as the velocity of the tip leakage flow increases, the leakage flow becomes more disordered due to the entry of the gas phase, significantly enhancing the scale of the TLV. Hence, the leakage rate and gas phase are the key factors affecting P_k . The results show that P_k increases with flow rate. However, the crucial factors affecting P_{wall} are the shear stress, leakage rate, and action area. As the flow rate increases, both the shear stress and leakage flow increase. The pump body wall area typically shows the high Φ_{wall} . However, as the flow rate increases, the initial point of the PTLV gradually moves to the trailing edge, and the area of high Φ_{wall} on the pump body wall decreases significantly. In addition, Φ_{wall} is affected by the gas phase attached to the walls in the impeller, which effectively reduces the action area between the liquid phase and the walls, resulting in a reduction in Φ_{wall} . Considering these factors, P_{wall} decreases gradually with increasing flow rate. It can be concluded that P_k plays the dominant role in the variation of P_{ens} .

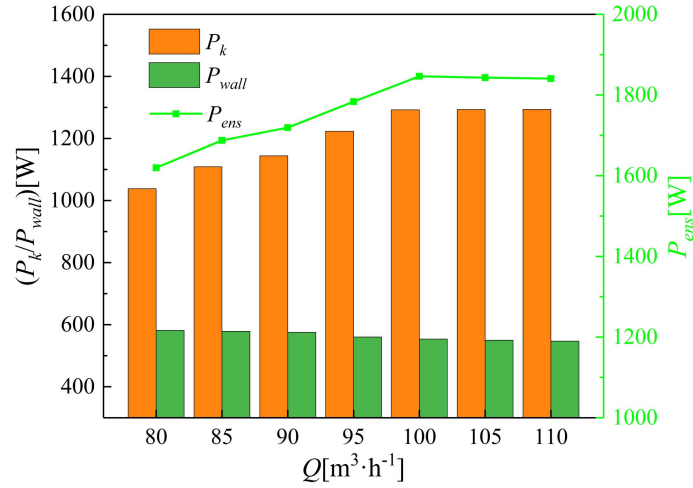


FIG. 11. Variation in entrophy dissipation power with flow rate.

5.2 Influence of tip clearance on entrophy dissipation

The results of steady simulations of the multiphase pump with varying tip clearances are presented in Table IV. The pressure loads on the PS and SS of the blade from the leading edge to the trailing edge tip to study the load distribution characteristics of the blades under different tip clearance conditions are shown in Fig. 12. The loading laws are consistent under different tip clearances from leading edge to trailing edge. The load on the PS of the blade increases suddenly at the 0–0.1 chord due to the impact of the impeller inlet flow. Further, the larger the tip clearance, the greater is the load on the blade. Along the 0.1–0.5 chord, the impeller blades continuously work on the fluid, transforming mechanical energy into the pressure energy of the fluid, thereby increasing the load on the PS gradually. In general, the pressure difference from the leading edge to the trailing edge increases at first, then reduces, reaching a maximum value at about the 0.5 chord. The entrophy dissipation is greatest at the point of maximum leakage flow intensity. In addition, as the tip clearance decreases, the pressure difference gradually increases, which increases the jet intensity. Careful observations show that, with increasing tip clearance, the load intersection between the PS and SS near the 0.1 chord gradually moves to the trailing edge, and the initial point of the PTLV is directly related to the pressure difference.

TABLE IV. Influence of the tip clearance on the entrophy dissipation power.

Number	Q[m³·h⁻¹]	Rtc[mm]	IGVF	P _k [W]	P _{wall} [W]	P _{ens} [W]
1	100	0.25	10%	661.02	568.95	1229.97
2	100	0.375	10%	875.82	559.07	1434.89
3	100	0.5	10%	1035.81	555.33	1591.14
4	100	0.625	10%	1147.05	554.88	1701.93
5	100	0.75	10%	1218.67	554.61	1773.28
6	100	0.875	10%	1265.01	554.28	1819.29
7	100	1.0	10%	1292.44	553.86	1846.30

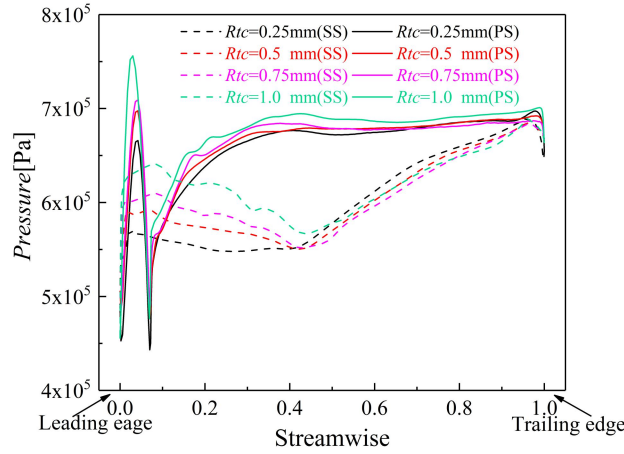


FIG. 12. Pressure load on the blade.

A total of four radial sections, denoted as RS₁–RS₄ in turn, are evenly distributed in the trajectory area of the PTLV, with the axial distance of the sections spanning only the flow passage between two blades. Three axial sections are selected with axial lengths of 10%, 50%, and 90% denoted as AS₁–AS₃, respectively, in the impeller between the inlet and outlet (Fig. 13). The volume enstrophy dissipation rate Φ_k and velocity vector under different tip clearances are displayed in Fig. 14. The TSV forms in the tip clearance region and the vortex region are quite similar to the enstrophy dissipation region. Therefore, the TSV in the tip clearance region is primarily responsible for energy dissipation. From RS₁ to RS₃, the pressure difference of the tip clearance increases gradually, and the vorticity and scale of the TSV increase accordingly, resulting in a continuous increase in Φ_k . As the tip clearance increases, the STL scale increases and extends to the SS of the blade under the same radial section. This proves that the enstrophy dissipation increases as the tip clearance increases. In addition, a smaller tip clearance results in stronger Φ_k near the pump body wall. When the clearance is small, the jet effect is significant on the walls, leading to the formation of small-scale vortices with counter-rotating directions in these regions and increasing the enstrophy dissipation.

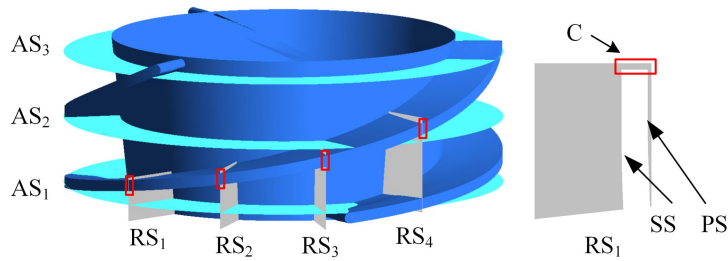


FIG. 13. Schematic diagram of the sections in the impeller.

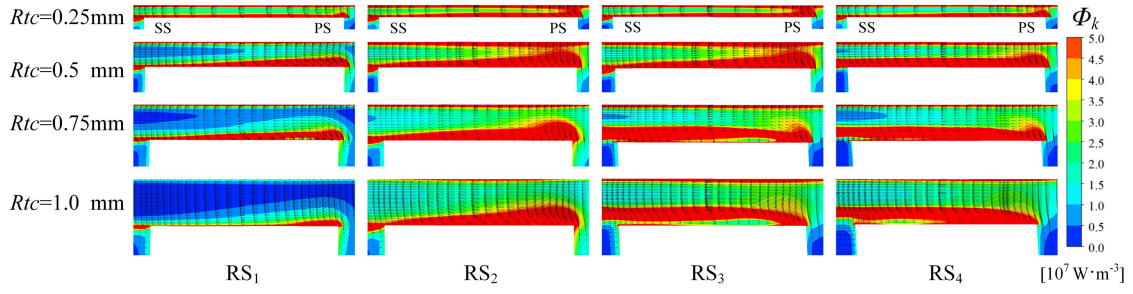


FIG. 14. Volume enstrophy dissipation rate and velocity vector in section C.

The streamline distributions on AS_1 – AS_3 are shown in Fig. 15. The velocity distributions on AS_1 – AS_3 are closely related to the flow pattern of the TLV along the direction of the main flow. The velocity is uniform at the impeller inlet (AS_1). However, there is a low-speed region near the PS tip due to the leakage flow from the SS to the PS. An LV is generated on the PS, and the velocity decreases. With increasing tip clearance, the velocity in the middle of the impeller passage gradually increases, while the low-speed region shrinks in size. Moreover, the scale of the LV gradually rises, and its core moves to the hub. Simultaneously, an obvious gradient appears in the velocity distribution in the middle of the impeller (AS_2). A high-speed region appears on the SS, while a large low-speed region is generated on the PS. The increasing scale due to the downstream movement of the PTLV along the SS enlarges the low-speed region. The high-speed and low-speed region gradually expands with increasing tip clearance. Furthermore, an obvious vortex core with low velocity appears when the tip clearance is 1 mm, with increasing velocity in the radial direction centered on the vortex core. Finally, the velocity tends to be uniform at the impeller outlet (AS_3), with high-speed regions appearing on both PS and SS. The velocity of the TV generated on the SS is the lowest.

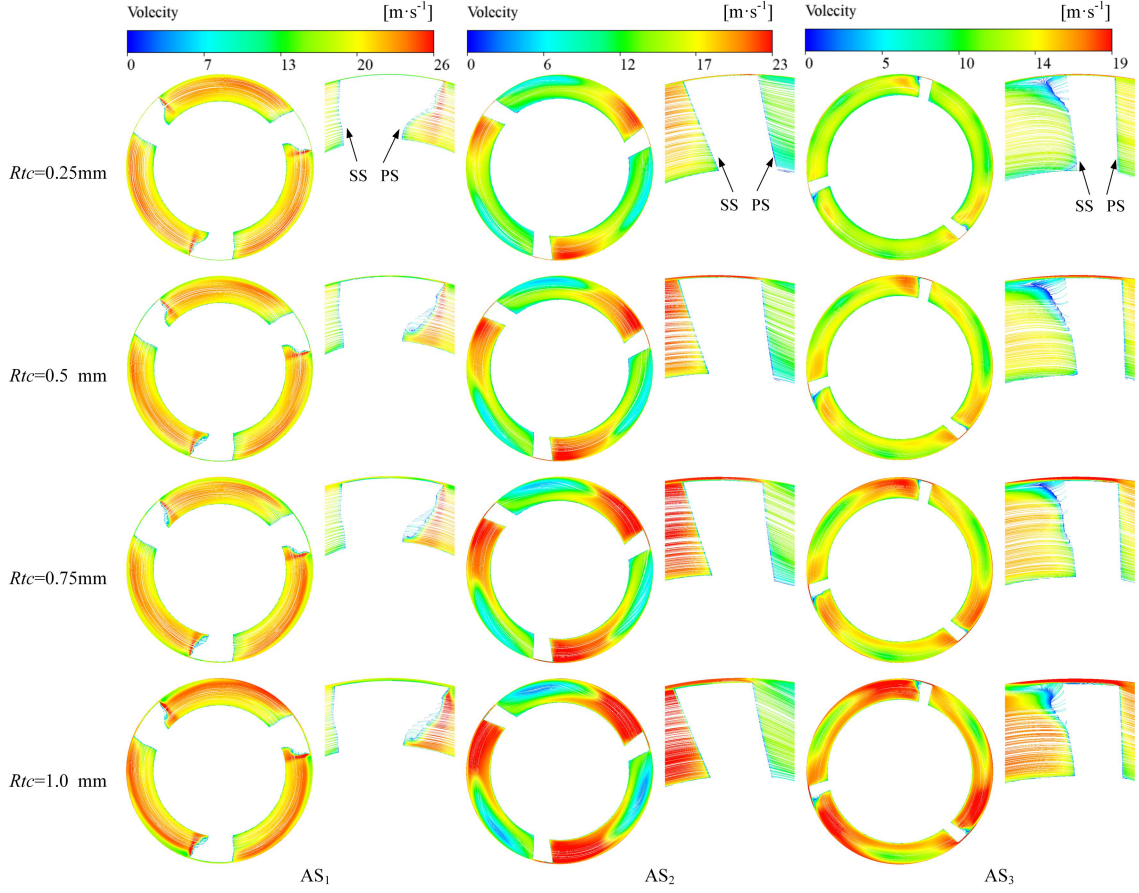


FIG. 15. Velocity streamlines on axial sections.

Figure 16 shows a histogram of the volume enstrophy dissipation power P_k , the wall enstrophy dissipation power P_{wall} , and variations in the total enstrophy dissipation power P_{ens} . Even minute variations in the tip clearance cause significant changes to the enstrophy dissipation in the impeller. As the tip clearance increases, the leakage rate increases, and the vorticity and scale of the TLV increase accordingly, thus, enhancing P_k . However, the volume increment decreases significantly, indicating that the sensitivity of P_k to the tip clearance gradually decreases. Moreover, when the tip clearance is small, the jet effect near the pump body wall is stronger, allowing the generation of small-scale vortex groups and resulting in an increase in P_{wall} . Therefore, P_{wall} decreases with increasing tip clearance. Thus, it can be concluded that P_{ens} increases as the tip clearance increases.

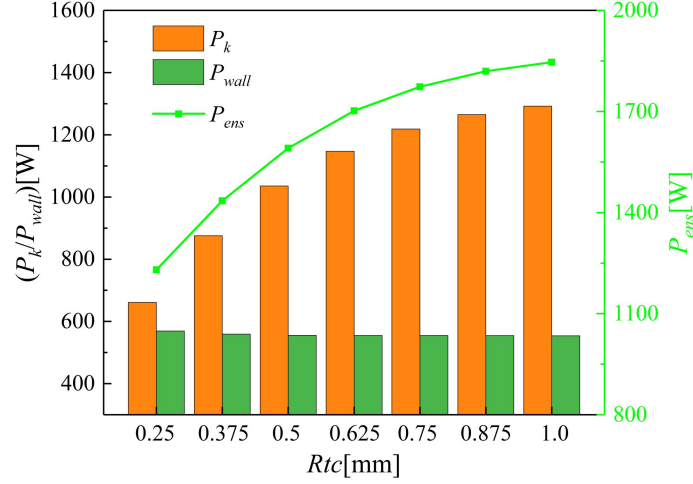


FIG. 16. Variation in entrophy dissipation power with tip clearance.

5.3 Influence of *IGVF* on entrophy dissipation

To quantitatively analyze the correlation between the pressure fluctuation and entrophy dissipation in the impeller of a multiphase pump, the pressure fluctuation intensity is introduced and given as follows:

$$\bar{p} = \frac{1}{N} \sum_{i=1}^n p_i, \quad (15)$$

$$\bar{p}' = \sqrt{\frac{1}{N} \sum_{i=1}^n (p_i - \bar{p})^2}, \quad (16)$$

where N is the number of sample points in the statistical period, p' is the pressure value of each time step, and \bar{p} is the arithmetic mean in the statistical period. The dimensionless pressure fluctuation intensity is given by

$$I_{PF} = \frac{\bar{p}'}{\frac{1}{2} \rho U_{ip}^2}, \quad (17)$$

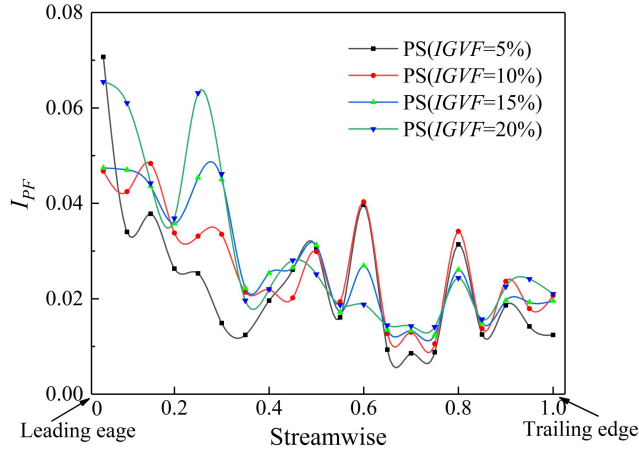
where U_{ip} is the tip circumferential velocity at a tip clearance of 1.0 mm (24.96 m/s in this study) and ρ is the density of the liquid.

Transient simulations were carried out with various values of the *IGVF*. The simulation results of the entrophy dissipation power are presented in Table V. Twenty monitoring points were evenly distributed between the leading and trailing edges of the PS and SS, and the curves of pressure fluctuation intensity I_{PF} under varied *IGVF* conditions were recorded (Fig. 17). It is apparent that the LV generated by the attack angle between the main flow direction and the setting angle of the blade deteriorates the flow pattern in the tip region, resulting in high I_{PF} values at the leading edge. Moreover, the flow state gradually becomes more stable from the leading edge to the trailing edge, while the TSV generated by the tip clearance disturbs the flow field, causing oscillations in I_{PF} on

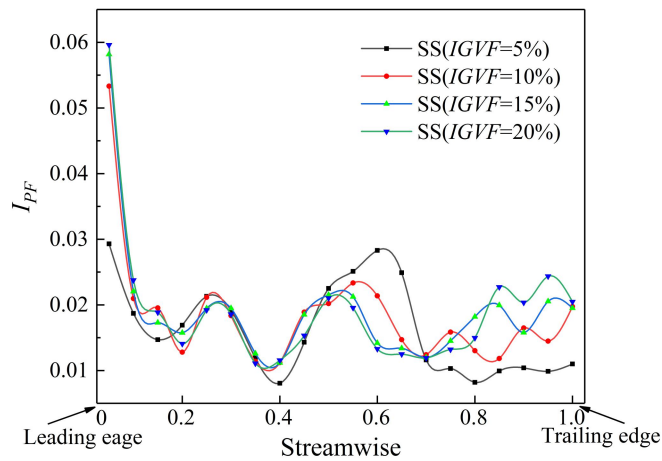
the PS. The increased I_{PF} in the PS with IGVF reflects the increase in the gas phase, enhancing the vorticity and scale of the TLV, which disorders the flow in the tip region and increases entropy dissipation. In particular, both the STL and TV cause drastic oscillations in the pressure fluctuations near the SS of the blade.

TABLE V. Influence of the $IGVF$ on the entropy dissipation power.

Number	$Q[\text{m}^3\cdot\text{h}^{-1}]$	$Rtc[\text{mm}]$	$IGVF$	$P_k[\text{W}]$	$P_{wall}[\text{W}]$	$P_{ens}[\text{W}]$
1	100	1.0	5%	1084.41	604.22	1688.63
2	100	1.0	7.5%	1138.97	576.15	1715.12
3	100	1.0	10%	1292.44	553.86	1846.30
4	100	1.0	12.5%	1385.75	543.77	1929.52
5	100	1.0	15%	1438.50	532.17	1970.67
6	100	1.0	17.5%	1593.84	525.36	2119.20
7	100	1.0	20%	1780.02	518.53	2298.55



(a)



(b)

FIG. 17. Pressure fluctuation intensity on the blade. (a) Pressure fluctuation intensity on the PS and (b) Pressure fluctuation intensity on the SS.

A line segment extending from the leading edge to the trailing edge in the tip clearance region

is generated and the three-dimensional streamlines released from this line segment along with the pressure fluctuation intensity I_{PF} on RS₁–RS₄ are shown in Fig. 18. This figure visualizes the process of TLV formation by the interaction between the tip leakage flow and the main flow. The PTLV originates at the leading edge and moves downstream along the direction of the main flow with a gradual decrease in its vorticity, whereas its vortex scale increases continuously. As the *IGVF* increases, the initial point of the PTLV gradually moves to the trailing edge, and its flow pattern becomes highly disordered, leading to enhanced enstrophy dissipation. When the patterns on RS₁–RS₄ are compared, it is found that I_{PF} is highest at the TLV core and gradually weakens along the flow direction, indicating that I_{PF} in the TLV core is closely related to vorticity. As the *IGVF* increases, the values of I_{PF} in the TLV core gradually decrease on RS₁–RS₃, whereas it gradually increases on RS₄ because of the vortex introduced by the PTLV near the PS.

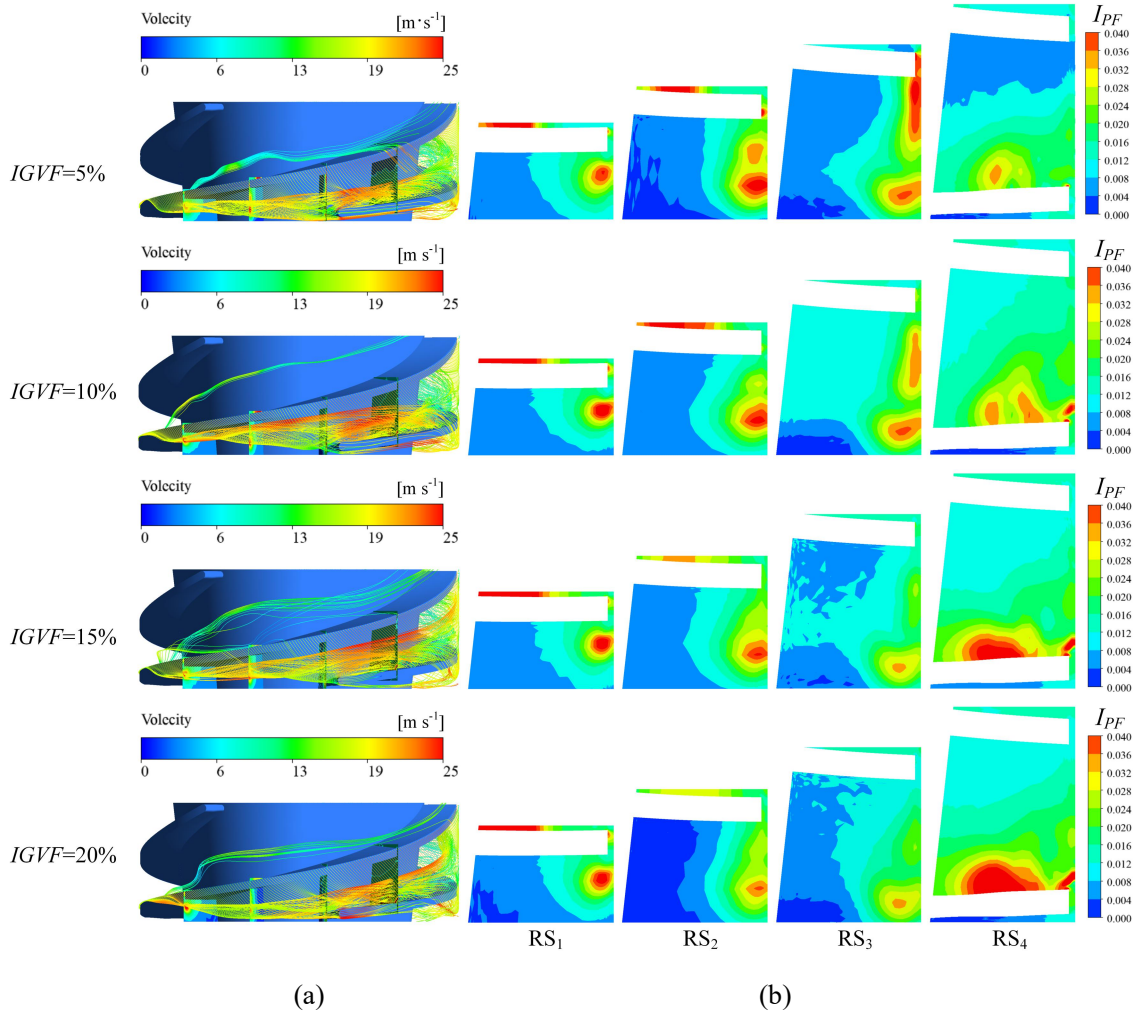


FIG. 18. Three-dimensional streamline in the impeller and pressure fluctuation intensity on radial sections. (a) Three-dimensional streamline and (b) pressure fluctuation intensity.

The pressure fluctuation intensity I_{PF} on the hub, blade, and shroud is displayed in Fig. 19. It can be observed that the distribution of I_{PF} on the impeller walls is associated with the TLV. First,

the LV disturbs the flow field at the leading edge of the blade and enhances I_{PF} . Later, the TSV is generated in the tip clearance region, and its core moves close to the tip and enhances I_{PF} (depicted with red areas). Finally, the PTLV breaks away from the SS and moves downstream close to the shroud, enhancing the pressure fluctuation intensity (depicted with black areas). The proportion of I_{PF} resulting from the PTLV and STLV gradually decreases with increasing $IGVF$. However, a region of high I_{PF} in the middle of the PS gradually expands with increasing $IGVF$. The I_{PF} is enhanced due to the generation of small-scale counter-rotating vortices resulting from the movement of PTLV along the PS.

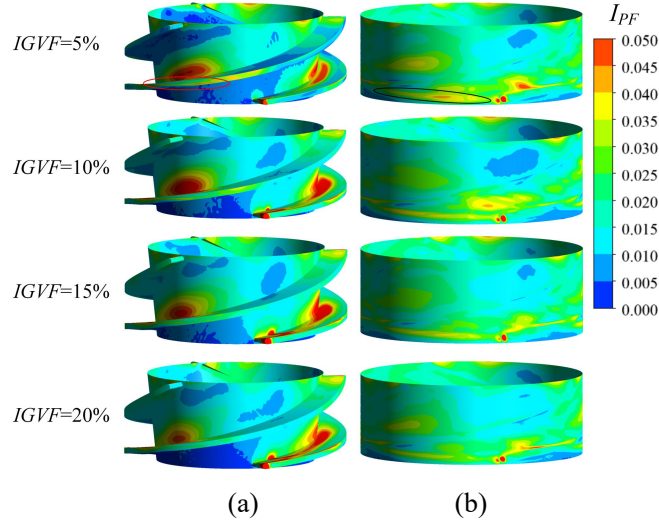


FIG. 19. Pressure fluctuation intensity on impeller walls. (a) Hub and blade and (b) shroud.

Figure 20 shows a histogram of the volume enstrophy dissipation power P_k , the wall enstrophy dissipation power P_{wall} , and the variations in the total enstrophy dissipation power P_{ens} . The flow pattern becomes more disordered in the impeller with increasing $IGVF$, and the PTLV scale increases. In particular, the STLV develops from a continuous sheet vortex to a scattered strip vortex and P_k increases significantly. The increment in P_k is smaller under lower $IGVF$ conditions (5%-15%), with a significant increase shown upon reaching 20% $IGVF$. This indicates that the performance of the multiphase pump decreases significantly under high $IGVF$ conditions. As the $IGVF$ increases, the area occupied by gas increases, thereby reducing the area occupied by liquid, causing P_{wall} to gradually decrease. Most importantly, the variation of P_{ens} grows exponentially, indicating that higher $IGVF$ conditions inevitably lead to greater energy loss. Therefore, the $IGVF$ is the key factor affecting the power performance of the impeller.

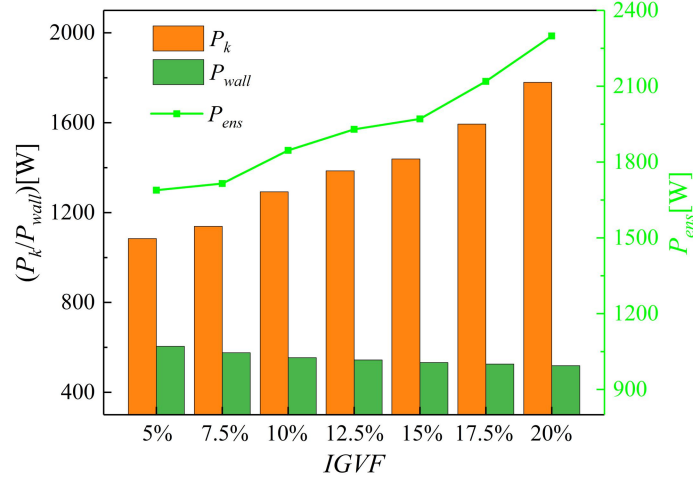


FIG. 20. Variation in entrophy dissipation power with $IGVF$.

6 PREDICTION MODELS

6.1 Simple nonlinear regression model

The flow rate, tip clearance, and $IGVF$ are important factors affecting entrophy dissipation in the impeller. Therefore, these three factors are selected to establish a simple nonlinear regression model to predict the variation law of entrophy dissipation. A simple linear regression model is introduced:

$$Y = \beta_0 + \beta_1 x + \varepsilon, \quad (18)$$

where $\varepsilon \sim N(0, \sigma^2)$ and β_0, β_1 are undetermined coefficients. Let (X_n, Y_n) be a set of samples and (x_n, y_n) be the observed values of that sample. For n groups of data (x_n, y_n) ,

$$y_i = \beta_0 + \beta_1 x_i + \varepsilon_i, \quad i = 1, 2, \dots, n, \quad (19)$$

where $\varepsilon_1, \varepsilon_2, \dots, \varepsilon_n$ are independent of each other. We hypothesize that

$$Y \sim N(\beta_0 + \beta_1 x \sigma^2), \quad E(Y) = \beta_0 + \beta_1 x. \quad (20)$$

Regression analysis provides an estimate of $\hat{\beta}_0, \hat{\beta}_1$ based on sample observations β_0, β_1 .

For a given value of x ,

$$Y = \hat{\beta}_0 + \hat{\beta}_1 x \quad (21)$$

Eq. (21) is called the linear regression equation of Y with respect to x as an estimate of $E(Y) = \beta_0 + \beta_1 x$. A nonlinear regression model can be established, when nonlinear relations can be transformed into linear relations.

The data in Tables III–V were processed and simple regression models for P_k , P_{wall} , and P_{ens} were obtained. These models are given in Table VI.

TABLE VI. Simple regression models.

Variable	Model	Expression
----------	-------	------------

	P_k	$-82204.44/Q + 2074.21$
Q	P_{wall}	$-1.3Q + 687.61$
	P_{ens}	$-70735.42/Q + 2515.92$
	P_k	$844.27Rtc^3 - 2790.32Rtc^2 + 3221.9Rtc + 16.41$
Rtc	P_{wall}	$4.91/Rtc + 547.64$
	P_{ens}	$708.12Rtc^3 - 2485.55Rtc^2 + 299.63Rtc + 623.74$
	P_k	$913.55e^{3.24IGVF}$
$IGVF$	P_{wall}	$432.5IGVF^{0.11}$
	P_{ens}	$1497.98e^{2.02IGVF}$

These regression models were subjected to statistical tests to determine their predictive power with the given sample data. The results are presented in Table VII. The goodness of fit of all regression models is greater than 0.9, indicating that they can explain more than 90% of the variation of variables. The variance significance of the regression models is less than 0.05, which proves that the functional relationships between the variables and the models are significant. In addition, the residuals of the regression models are small and conform to a normal distribution.

TABLE VII. Statistical tests of regression models.

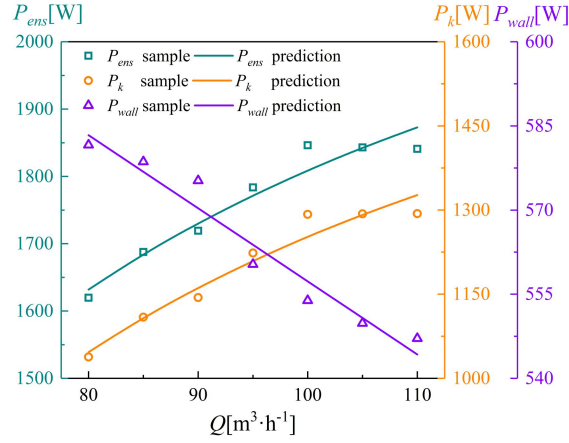
Variable	Model	R^2	F	Sig.	SSE
Q	P_k	0.949	92.60	0	3289.08
	P_{wall}	0.949	93.62	0	63.50
	P_{ens}	0.940	78.51	0	2872.46
Rtc	P_k	1.000	—	0	0
	P_{wall}	0.924	60.84	0.01	13.43
	P_{ens}	1.000	—	0	0
$IGVF$	P_k	0.985	333.38	0	5492.29
	P_{wall}	0.995	1057.42	0	25.80
	P_{ens}	0.971	168.48	0	8453.41

The predicted enstrophy dissipation power under different variables is shown in Fig. 21. Figure 21(a) shows that there is an inverse relationship between P_k and Q . P_k gradually increase with Q , nevertheless its rate of increment decreases. Besides, there is a negative linear correlation between P_{wall} and Q . The average errors of P_k , P_{wall} , and P_{ens} are 1.35%, 1.84%, and 0.87%, respectively, indicating that the regression models have high prediction accuracy.

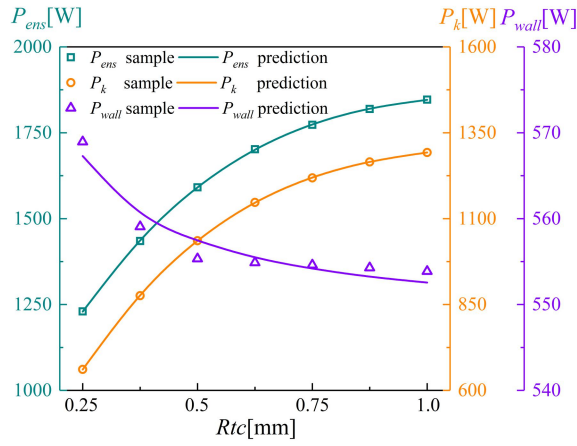
As shown in Fig. 21(b), both P_k and P_{ens} have a cubic relationship with Rtc , whereas P_{wall} and Rtc are inversely related. Both P_k and P_{ens} gradually increase at a decreasing rate as Rtc increases, whereas P_{wall} converges to a definite value. The average errors of P_k , P_{wall} , and P_{ens} are 0%, 0.23%, and 0%, respectively. The predicted values almost coincide with the samples, which proves that the prediction effect is excellent.

Similarly, Fig. 21(c) shows that both P_k and P_{ens} are exponential functions of $IGVF$, whereas there is a power function relationship between P_{wall} and $IGVF$. With increasing $IGVF$, P_k and P_{ens}

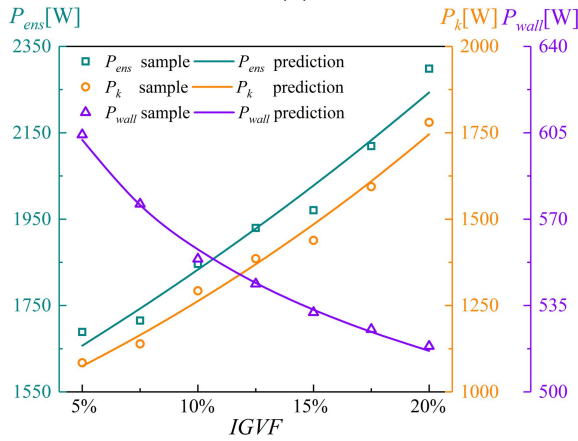
increase rapidly, while P_{wall} decreases gradually. The average errors of P_k , P_{wall} , and P_{ens} are 1.83%, 0.28%, and 1.46%, respectively. These results suggest that the prediction accuracy is high.



(a)



(b)



(c)

FIG. 21. Prediction curves of the entrophy dissipation power with different variables. (a) Flow rate, (b) tip clearance, and (c) $IGVF$.

6.2 Multiple nonlinear regression model

The flow rate, tip clearance, and $IGVF$ change simultaneously and affect one another. Therefore,

16 conditions were selected to obtain sample values of the enstrophy dissipation power in the impeller. The results are listed in Table VIII.

TABLE VIII. Influence of multiple variables on enstrophy dissipation power.

Number	$Q[\text{m}^3\cdot\text{h}^{-1}]$	$Rtc[\text{mm}]$	$IGVF$	$P_k[\text{W}]$	$P_{wall}[\text{W}]$	$P_{ens}[\text{W}]$
1	80	0.25	5%	629.30	623.49	1252.79
2	80	0.5	10%	979.24	585.42	1564.66
3	80	0.75	15%	1284.99	562.57	1847.56
4	80	1.0	20%	1700.24	539.93	2240.17
5	90	0.25	10%	655.12	581.58	1236.70
6	90	0.5	15%	1186.31	551.28	1737.59
7	90	0.75	20%	1565.89	531.08	2096.97
8	90	1.0	5%	1042.88	606.44	1649.32
9	100	0.25	15%	1104.61	555.85	1660.46
10	100	0.5	20%	1507.24	523.40	2030.64
11	100	0.75	5%	990.60	595.88	1586.48
12	100	1.0	10%	1292.44	553.86	1846.30
13	110	0.25	20%	1676.91	524.68	2201.59
14	110	0.5	5%	811.06	571.40	1382.46
15	110	0.75	10%	1161.59	553.14	1714.73
16	110	1.0	15%	1579.37	529.23	2108.60

To evaluate the variation law of enstrophy dissipation power under the influence of multiple variables, a suitable multiple nonlinear regression model is derived. A mathematical linear regression model covering p variables has the form

$$y = \alpha_0 + \alpha_1 x_1 + \alpha_2 x_2 + \cdots + \alpha_p x_p + \varepsilon, \quad (22)$$

where ε is a random variable. The conditional expectation of Eq. (22) is

$$E(y) = \alpha_0 + \alpha_1 x_1 + \alpha_2 x_2 + \cdots + \alpha_p x_p. \quad (23)$$

Estimates of the true values $\alpha_0, \alpha_1, \dots, \alpha_p$ obtained from the sample data are denoted as $\hat{\alpha}_0, \hat{\alpha}_1, \dots, \hat{\alpha}_p$. A multiple linear regression model is obtained as

$$\hat{y} = \hat{\alpha}_0 + \hat{\alpha}_1 x_1 + \hat{\alpha}_2 x_2 + \cdots + \hat{\alpha}_p x_p. \quad (24)$$

Using the data in Table VIII, the independent variables are first linearized. Then, a multiple linear regression method is used to fit the linearized variables. Finally, multiple nonlinear regression models are established for P_k , P_{wall} , and P_{ens} . These can be expressed as follows:

$$P_k = 5.88Q + 516.62Rtc + 285.34e^{7IGVF} - 421.07, \quad (25)$$

$$P_{wall} = -1.1Q + 4.5 / Rtc - 454.72IGVF + 713.85, \quad (26)$$

$$P_{ens} = 4.78Q + 500.89Rtc + 197.88e^{8IGVF} + 399.99. \quad (27)$$

The results of statistical tests performed on these regression models are presented in Tables IX and X. Table IX shows that the adjusted R^2 values of P_k , P_{wall} , and P_{ens} exceed 0.9, indicating better

goodness of fit. Moreover, the F statistics of the regression models are high, and the correlation between the explained and explanatory variables is significant. The Durbin–Watson (DW) values of P_k and P_{ens} are close to 2, indicating that the residual sequence has no autocorrelation. However, the DW value of P_{wall} is 2.443, suggesting that the residual sequence has a negative autocorrelation, which is within the acceptable range. Table X shows that the significance of the T statistics between variables is less than 0.05, suggesting the significant effect of the regression model. The multicollinearity, which refers to the phenomenon of linear correlations between explanatory variables, is measured by the tolerance and its reciprocal, the variance inflation factor (VIF). The tolerance and VIF values of all variables are 1 for P_k , P_{wall} , and P_{ens} , inferring that there is no collinearity between variables. The sample values are compared with the predicted values for multiple regression models in Fig. 22. The average errors of P_k , P_{wall} , and P_{ens} are 5.42%, 0.07%, and 3.49%, respectively, indicating that the multiple regression models achieve high predictive accuracy.

TABLE IX. Significance test results.

Model	Adjusted R^2	F	Sig.	DW
P_k	0.938	76.64	0	1.93
P_{wall}	0.961	125.45	0	2.44
P_{ens}	0.923	61.35	0	2.02

TABLE X. Correlation test between variables.

Model	Variable	Coefficient	T	Sig.	Tol	VIF
P_k	Q	5.88	3.07	0.01	1	1
	Rtc	516.62	6.76	0	1	1
	$IGVF$	285.34	13.22	0	1	1
P_{wall}	Q	-1.10	-8.31	0	1	1
	Rtc	4.50	3.54	0.004	1	1
	$IGVF$	-454.72	-17.17	0	1	1
P_{ens}	Q	4.78	2.43	0.032	1	1
	Rtc	500.89	6.37	0	1	1
	$IGVF$	197.88	11.73	0	1	1

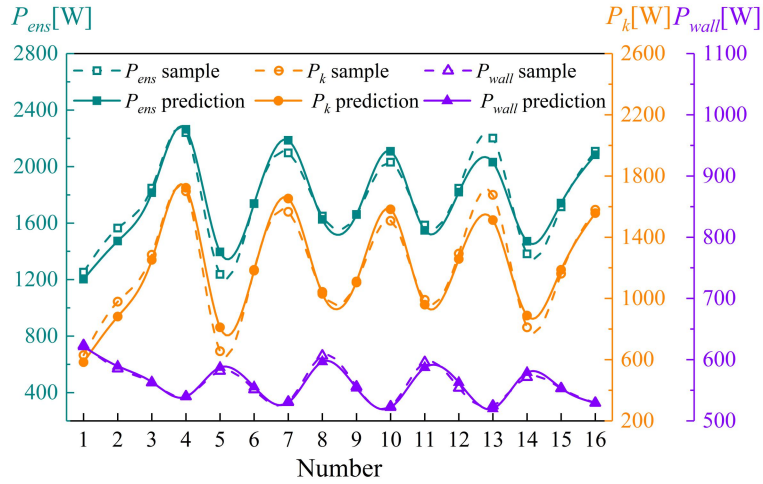


FIG. 22. Comparison of sample values and predicted values given by multiple regression models.

7 CONCLUSION

In the present work, the enstrophy dissipation theory is innovatively applied to quantitatively study the energy dissipation of the TLV. The flow rate, tip clearance, and $IGVF$ play a crucial role in impacting the flow pattern and enstrophy dissipation of the TLV. Simple and multiple nonlinear regression models for enstrophy dissipation are established considering the flow rate, tip clearance, and $IGVF$ as independent variables, to accurately predict the enstrophy dissipation law. The results of the numerical simulation and experiment measurement are compared to verify the reliability and accuracy of the numerical simulation. The tip leakage flow interacts with the main flow and evolves into the complex TLV structures, such as LV, TSV, STLV, PTLV, and TV. The streamline at the tip clearance region depicts a spiral pattern of the intertwined vortex filaments. TLV causes unstable flow and leads to enstrophy dissipation in the impeller. Increases in flow rate, tip clearance, and $IGVF$ exacerbate the TLV pattern and raise the TLV scale, resulting in a gradual increase in volume enstrophy dissipation and a gradual decrease in wall enstrophy dissipation. The initial point of the PTLV gradually moves from the leading edge to the trailing edge of the blade as the flow rate increases, decreasing the separation angle between the PTLV trajectory and the blade. It is observed that the distribution of the gas phase near the shroud is associated with the TLV trajectory. Gas void fraction is highest at the core of the TLV and gradually decreases along the radial direction with the vortex core as the center. The pressure difference from the leading edge to the trailing edge initially increases, reaching a maximum value at about the 0.5 chord, then reduces. The enstrophy dissipation is greatest at the point of maximum leakage flow intensity. The jet effect on the walls is significant when the clearance is small, leading to the formation of small-scale vortices with counter-rotating directions in these regions boosting the enstrophy dissipation. As the tip clearance increases, the TSV scale increases and extends to the SS, and the velocity gradient in the impeller passage increases. As the $IGVF$ increases, the vorticity and scale of the STLV and pressure fluctuation intensity increase, disorganizing the flow pattern in the tip region. In particular, the STLV develops

from a continuous sheet vortex to a scattered strip vortex, significantly increasing the volume enstrophy dissipation power. However, the pressure fluctuation intensity gradually decreases on the hub and shroud and reduces the wall enstrophy dissipation power. Moreover, statistical tests show that simple and multiple nonlinear regression models have the ability to predict the enstrophy dissipation of the TLV accurately, which can form the basis for practical engineering applications.

Acknowledgements

The authors sincerely thanks to Professor Xiaobing Liu from Xihua University for their critical discussion during the experiment.

Authors' Contributions

Zekui Shu and Guangtai Shi proposed the simulation method and designed the experiment; Xin Yao, Guodong Sun and Sijia Tao performed the experiment; Zekui Shu completed the numerical simulations; Zekui Shu and Guangtai Shi analyzed the data and wrote the paper.

Authors' Information

Zekui Shu, born in 1994, is currently a master candidate at Key Laboratory of Fluid Machinery and Engineering (Xihua University), Sichuan Province, China.

Guangtai Shi, born in 1985, is currently an associate professor at Key Laboratory of Fluid Machinery and Engineering (Xihua University), Sichuan Province, China. He received her PhD degree from Lanzhou University of Technology, in 2015. He studies the flow theory and mechanism of multiphase flow.

Xin Yao, born in 1999, is currently a master candidate at Key Laboratory of Fluid Machinery and Engineering (Xihua University), Sichuan Province, China.

Guodong Sun, born in 1994, is currently a master candidate at Key Laboratory of Fluid Machinery and Engineering (Xihua University), Sichuan Province, China.

Sijia Tao, born in 1998, is currently a master candidate at Key Laboratory of Fluid Machinery and Engineering (Xihua University), Sichuan Province, China.

Competing Interests

The authors declare no competing financial interests.

Availability of data and materials

The data that support the findings of this study are available from the corresponding author upon reasonable request.

Funding

This work was supported by the Open Research Fund Program of State Key Laboratory of Hydrosience and Engineering (sklhse-2021-E-03); the Key scientific research fund of Xihua University of China (Z1510417); the Central Leading Place Scientific and Technological Development Funds for Surface Project (2021ZYD0038); the National Key Research and Development Program (2018YFB0905200), and the Graduate Innovation Fund in 2021 (YCJJ2021059).

REFERENCES

- ¹J. Suh, J. Kim, Y. Choi, W. Joo, and K. Lee, “A study on numerical optimization and performance verification of multiphase pump for offshore plant,” *Proc. Inst. Mech. Eng., Part A* **231**(5), 382 (2017).
- ²M. Liu, L. Tan, Y. Xu, and S. Cao, “Optimization design method of multi-stage multiphase pump based on Oseen vortex,” *J. Petrol. Sci. Eng.* **184**, 106532 (2020).
- ³W. Xiao and L. Tan, “Design method of controllable velocity moment and optimization of pressure fluctuation suppression for a multiphase pump,” *Ocean Eng.* **220**, 108402 (2021).
- ⁴M. Liu, L. Tan, and S. Cao, “Influence of viscosity on energy performance and flow field of a multiphase pump,” *Renew. Energ.* **162**, 1151 (2020).
- ⁵J. Zhang, S. Cai, Y. Li, Y. Li, and Y. Zhang, “Optimization design of multiphase pump impeller based on combined genetic algorithm and boundary vortex flux diagnosis,” *J. Hydrodyn.* **29**(6), 1023 (2017).
- ⁶J. Zhang, H. Zhu, C. Yang, Y. Li, and H. Wei, “Multi-objective shape optimization of helico-axial multiphase pump impeller based on NSGA-II and ANN,” *Energ. Convers. Manage.* **52**(1), 538 (2011).
- ⁷G. Shi, Z. Liu, Y. Xiao, H. Li, and X. Liu, “Tip leakage vortex trajectory and dynamics in a multiphase pump at off-design condition,” *Renew. Energ.* **150**, 703 (2020).
- ⁸T. Lei, X. Zhifeng, L. Yabin, H. Yue, and X. Yun, “Influence of T-shape tip clearance on performance of a mixed-flow pump,” *Proc. Inst. Mech. Eng., Part A* **232**(4), 386 (2018).
- ⁹Q. Guo, L. Zhou, and Z. Wang, “Numerical evaluation of the clearance geometries effect on the flow field and performance of a hydrofoil,” *Renew. Energ.* **99**, 390 (2016).
- ¹⁰L. Ji, W. Li, and W. Shi, “Influence of tip leakage flow and inlet distortion flow on a mixed-flow

pump with different tip clearances within the stall condition,” Proc. Inst. Mech. Eng., Part A **234**(4), 433 (2020).

¹¹M. Liu, L. Tan and S. Cao, "Dynamic mode decomposition of gas-liquid flow in a rotodynamic multiphase pump," Renew. Energ. **139**, 1159-1175 (2019).

¹²Q. Wang and W. Yao, "Computation and validation of the interphase force models for bubbly flow," Int. J. Heat Mass Tran. **98**, 799-813 (2016).

¹³G. Shi, Z. Liu, Y. Xiao, H. Yang, H. Li, and X. Liu, "Effect of the inlet gas void fraction on the tip leakage vortex in a multiphase pump," Renew. Energ. **150**, 46-57 (2020).

¹⁴J. Zhang, H. Fan, W. Zhang, and Z. Xie, "Energy performance and flow characteristics of a multiphase pump with different tip clearance sizes," Adv. Mech. Eng. **11** (1), 2072051423 (2019).

¹⁵J. Zhang, S. Cai, Y. Li, H. Zhu, and Y. Zhang, "Visualization study of gas-liquid two-phase flow patterns inside a three-stage rotodynamic multiphase pump," Exp. Therm. Fluid Sci. **70**, 125 (2016).

¹⁶Y. Shi, H. Zhu, J. Zhang, J. Zhang, and J. Zhao, "Experiment and numerical study of a new generation three-stage multiphase pump," J. Petrol. Sci. Eng. **169**, 471 (2018).

¹⁷J. Zhang, S. Cai, H. Zhu, and Y. Zhang, "Experimental investigation of the flow at the entrance of a rotodynamic multiphase pump by visualization," J. Petrol. Sci. Eng. **126**, 254 (2015).

¹⁸W. Zhang, B. Zhu, and Z. Yu, "Characteristics of bubble motion and distribution in a multiphase rotodynamic pump," J. Petrol. Sci. Eng. **193**, 107435 (2020).

¹⁹W. Zhang, X. Xie, B. Zhu, and Z. Ma, "Analysis of phase interaction and gas holdup in a multistage multiphase rotodynamic pump based on a modified Euler two-fluid model," Renew. Energ. **164**, 1496 (2021).

²⁰G. Shi, Z. Liu, Y. Xiao, Z. Wang, Y. Luo, and K. Luo, "Energy conversion characteristics of multiphase pump impeller analyzed based on blade load spectra," Renew. Energ. **157**, 9 (2020).

²¹G. Shi, Z. Liu, Y. Xiao, H. Li, and X. Liu, "Velocity characteristics in a multiphase pump under different tip clearances," Proc. Inst. Mech. Eng., Part A **235**(3), 454 (2021).

²²G. Shi, Z. Liu, Y. Xiao, H. Yang, H. Li, and X. Liu, "Effect of the inlet gas void fraction on the tip leakage vortex in a multiphase pump," Renew. Energ. **150**, 46 (2020).

²³A. Pogorelov, M. Meinke and W. Schröder, "Cut-cell method based large-eddy simulation of tip-leakage flow," Phys. Fluids **27** (7), 75106 (2015).

- ²⁴J. Fang, Y. Gao, Y. Liu, L. Lu, Y. Yao, and C. Le Ribault, "Direct numerical simulation of a tip-leakage flow in a planar duct with a longitudinal slit," *Phys. Fluids* **31** (12), 125108 (2019).
- ²⁵Y. Han and L. Tan, "Influence of rotating speed on tip leakage vortex in a mixed flow pump as turbine at pump mode," *Renew. Energ.* **162**, 144 (2020).
- ²⁶Y. Han and L. Tan, "Dynamic mode decomposition and reconstruction of tip leakage vortex in a mixed flow pump as turbine at pump mode," *Renew. Energ.* **155**, 725 (2020).
- ²⁷H. Wu, R. L. Miorini, D. Tan, and J. Katz, "Turbulence Within the Tip-Leakage Vortex of an Axial Waterjet Pump," *AIAA J.* **50**(11), 2574 (2012).
- ²⁸H. Wu, R. L. Miorini, and J. Katz, "Measurements of the tip leakage vortex structures and turbulence in the meridional plane of an axial water-jet pump," *Exp. Fluids* **50**(4), 989 (2011).
- ²⁹H. Wu, D. Tan, R. L. Miorini, and J. Katz, "Three-dimensional flow structures and associated turbulence in the tip region of a waterjet pump rotor blade," *Exp. Fluids* **51**(6), 1721 (2011).
- ³⁰Y. Liu and L. Tan, "Spatial-Temporal Evolution of Tip Leakage Vortex in a Mixed-Flow Pump with Tip Clearance," *J. Fluid. Eng.* **141**(8), 081302 (2019).
- ³¹Y. Liu and L. Tan, "Tip clearance on pressure fluctuation intensity and vortex characteristic of a mixed flow pump as turbine at pump mode," *Renew. Energ.* **129**, 606 (2018).
- ³²Y. Liu and L. Tan, "Theoretical Prediction Model of Tip Leakage Vortex in a Mixed Flow Pump with Tip Clearance," *J. Fluid. Eng.* **142**(2), 021203 (2020).
- ³³H. Y. Cheng, X. R. Bai, X. P. Long, B. Ji, X. X. Peng, and M. Farhat, "Large eddy simulation of the tip-leakage cavitating flow with an insight on how cavitation influences vorticity and turbulence," *Appl. Math. Model.* **77**, 788 (2020).
- ³⁴H. Cheng, X. Long, B. Ji, X. Peng, and M. Farhat, "LES investigation of the influence of cavitation on flow patterns in a confined tip-leakage flow," *Ocean Eng.* **186**, 106115 (2019).
- ³⁵M. Xu, H. Cheng, B. Ji, and X. Peng, "LES of tip-leakage cavitating flow with special emphasis on different tip clearance sizes by a new Euler-Lagrangian cavitation model," *Ocean Eng.* **213**, 107661 (2020).
- ³⁶T. Lei, X. Zhifeng, L. Yabin, H. Yue, and X. Yun, "Influence of T-shape tip clearance on performance of a mixed-flow pump," *Proc. Inst. Mech. Eng., Part A* **232**(4), 386 (2018).
- ³⁷Z. Huang, Z. Huang, and H. Fan, "Influence of C groove on energy performance and noise source

- of a NACA0009 hydrofoil with tip clearance,” *Renew. Energ.* **159**, 726 (2020).
- ³⁸Y. Huang, D. Zhang, F. Wang, G. Zhang, and B. P. M. B. van Esch, “Vortex suppression of the tip leakage flow over a NACA0009 hydrofoil via a passive jet induced by the double-control-hole,” *Ocean Eng.* **237**, 109647 (2021).
- ³⁹S. Jiang, F. Chen, J. Yu, S. Chen, and Y. Song, “Treatment and optimization of casing and blade tip for aerodynamic control of tip leakage flow in a turbine cascade,” *Aerosp. Sci. Technol.* **86**, 704 (2019).
- ⁴⁰L. Shi, D. Zhang, Y. Jin, W. Shi, and B. P. M. Bart Van Esch, “A study on tip leakage vortex dynamics and cavitation in axial-flow pump,” *Fluid Dyn. Res.* **49**(3), 35504 (2017).
- ⁴¹S. Xi, Z. Desheng, X. Bin, S. Weidong, and B. P. M. Bart Van Esch, “Experimental and numerical investigation on the effect of tip leakage vortex induced cavitating flow on pressure fluctuation in an axial flow pump,” *Renew. Energ.* **163**, 1195 (2021).
- ⁴²G. Shi, Z. Liu, Y. Xiao, Z. Wang, Y. Luo, and K. Luo, “Energy conversion characteristics of multiphase pump impeller analyzed based on blade load spectra,” *Renew. Energ.* **157**, 9 (2020).
- ⁴³H. Hou, Y. Zhang, Z. Li, T. Jiang, J. Zhang, and C. Xu, “Numerical analysis of entropy production on a LNG cryogenic submerged pump,” *J. Nat. Gas Sci. Eng.* **36**, 87 (2016).
- ⁴⁴J. Huang, K. Li, G. Chen, J. Gong, Q. Zhang, and Y. Wang, “Design and experimental verification of variable-structure vortex tubes for valveless piezoelectric pump translating high-viscosity liquid based on the entropy generation,” *Sensors Actuat. A–Phys.* **331**, 112973 (2021).
- ⁴⁵D. Li, H. Wang, Y. Qin, L. Han, X. Wei, and D. Qin, “Entropy production analysis of hysteresis characteristic of a pump–turbine model,” *Energ. Convers. Manage.* **149**, 175 (2017).
- ⁴⁶C. Wang, Y. Zhang, J. Zhang, and J. Zhu, “Flow pattern recognition inside a rotodynamic multiphase pump via developed entropy production diagnostic model,” *J. Petrol. Sci. Eng.* **194**, 107467 (2020).
- ⁴⁷L. Ji, W. Li, W. Shi, F. Tian, and R. Agarwal, “Effect of blade thickness on rotating stall of mixed-flow pump using entropy generation analysis,” *Energy* **236**, 121381 (2021).
- ⁴⁸L. Ji, W. Li, W. Shi, H. Chang, and Z. Yang, “Energy characteristics of mixed-flow pump under different tip clearances based on entropy production analysis,” *Energy* **199**, 117447 (2020).
- ⁴⁹J. Wu, Y. Zhou, and M. Fan, “A note on kinetic energy, dissipation and enstrophy,” *Phys. Fluids*

11(2), 503 (1999).

⁵⁰O. R. H. Buxton and B. Ganapathisubramani, “Amplification of enstrophy in the far field of an axisymmetric turbulent jet,” *J. Fluid Mech.* **651**, 483 (2010).

⁵¹R. Benzi, L. Biferale, E. Calzavarini, D. Lohse, and F. Toschi, “Velocity-gradient statistics along particle trajectories in turbulent flows: the refined similarity hypothesis in the Lagrangian frame,” *Phys. Rev. E Stat. Nonlin. Soft Matter Phys.* **80**(6 Pt 2), 66318 (2009).

⁵²A. R. Varma, U. Ahmed, and N. Chakraborty, “Effects of body forces on vorticity and enstrophy evolutions in turbulent premixed flames,” *Phys. Fluids* **33**(3), 035102 (2021).

⁵³M. M. Neamtu-Halic, J. P. Mollicone, M. van Reeuwijk, and M. Holzner, “Role of vortical structures for enstrophy and scalar transport in flows with and without stable stratification,” *J. Turbul.* **22**(7), 393 (2021).

⁵⁴T. Lin, X. Li, Z. Zhu, J. Xie, Y. Li, and H. Yang, “Application of enstrophy dissipation to analyze energy loss in a centrifugal pump as turbine,” *Renew. Energ.* **163**, 41 (2021).

⁵⁵J. Suh, J. Kim, Y. Choi, J. Kim, W. Joo, and K. Lee, “Development of numerical Eulerian-Eulerian models for simulating multiphase pumps,” *J. Petrol. Sci. Eng.* **162**, 588-601 (2018).

⁵⁶F. Kock and H. Herwig, “Local entropy production in turbulent shear flows: a high-Reynolds number model with wall functions,” *Int. J. Heat Mass Transf.* **47**(10–11), 2205 (2004).